JOURNAL OF COMPUTATIONAL PHYSICS **129,** 57–73 (1996)
ARTICLE NO. 0233

Modeling Biofilm Processes Using the Immersed Boundary Method

Robert Dillon,* Lisa Fauci,* Aaron Fogelson,† and Donald Gaver III‡

*Department of Mathematics, Tulane University, New Orleans, Louisiana 70118; †Department of Mathematics, University of Utah, Salt Lake City, Utah 84102; and ‡Department of Biomedical Engineering, Tulane University, New Orleans, Louisiana 70118

Received November 28, 1995; revised July 3, 1996

Biofilm processes are of interest to researchers in a variety of fields including bioremediation, oil recovery, wastewater treatment, medicine, and dentistry. In this paper we describe how this complex, dynamic, fluid–structure interaction can be modeled successfully using the *immersed boundary method*. The model presented here includes the coupling of hydrodynamics; substrate reaction, diffusion, and convection; as well as the chemotactic response of swimming microbes. Cell–cell aggregation and cell–substratum adhesion are modeled by generating appropriate binding forces between discrete representations of organisms that may hold them together, or if fluid stresses are large, may yield and release the organisms. In this paper, we show two-dimensional numerical simulations to demonstrate several different types of scenarios that may be modeled using immersed boundary methods. These simulations indicate the variety of different phenomena one might expect in biofilm processes.

1. INTRODUCTION

An important aspect of microbial processes is the propensity of cells to aggregate and adhere to each other and bind to a surface. The adsorbed cells may produce a matrix of extracellular polymer substance (EPS) binding the cells together. A *biofilm* consists of the adsorbed cells in association with EPS. The accumulation of biofilm depends on hydrodynamic processes that bring cells to the biofilm surface, physicochemical properties that determine the propensity of microbes to attach to the biofilm, and environmental characteristics such as substrate concentrations which determine growth characteristics. Cells may also be removed from the biofilm by biological processes or flow properties that lead to desorption and detachment. Biofilm growth changes the geometry and alters the fluid flow. At the same time, substrates are transported from the bulk fluid to the biofilm by diffusion and advection processes and are consumed by the cells.

The purpose of this paper is to show that this complex and dynamic system can be modeled successfully using the *immersed boundary method*. This method, first introduced by Peskin [20] to model blood flow in the heart, has evolved into a general method that can be used to study flows interacting with complex elastic structures. The distinctive feature of this method is the treatment of a complex structure, whether it is a heart valve, a flagellum, or an aggregate of cells, as a region in the fluid in which additional elastic forces are applied. The name of the method derives from the fact that such structures are often modeled as thin elastic membranes immersed in the fluid and bounding regions of the fluid. Because the presence of the elastic structures influences the fluid only through these forces, the fluid dynamics equations can be solved efficiently on a square or cubic lattice, unaffected by the geometry of the elastic structures which themselves may be complicated and time-dependent. Using this Eulerian description of the fluid doman, and a Lagrangian description of the elastic structures, the entire fluid velocity field is constructed during each time step. The local velocities at points of the immersed boundaries are interpolated from the fluid grid velocities, and their positions are updated accordingly. Moreover, since the fluid velocity field is already available, the coupling of the fluid equations with one or more chemical advection–reaction–diffusion equations is easily achieved.

The biofilm model presented here includes the coupling of hydrodynamics, substrate reaction, diffusion and convection; as well as the chemotactic response of swimming microbes. Cell–cell aggregation and cell–substratum (i.e., cell–surface) adhesion are modeled by generating appropriate binding forces between discrete representations of organisms, that may hold them together, or, if fluid stresses are large, may yield and release the organisms.

In a laboratory environment, it is difficult to alter a particular biological parameter such as cell motility without changing other parameters at the same time. For example, in one study of bacterial penetration through porous media, the penetration rate of a motile species was compared with the rate of a mutant lacking motility. However, the nonmotile mutant exhibited a significantly higher growth rate than the motile variety. This difference in growth rates complicated the interpretation of the experimental results [22]. In our computational model, we are able to systemati-

0021-9991/96 $18.00

cally vary the parameters which control cell–cell and cell–substratum attraction, cell motility, substrate diffusion rates, microbial uptake rates, as well as the chemotactic response of cells to the evolving substrate field. The ability to independently vary specific parameters permits evaluation of the relative importance of different mechanisms. This provides a tool that may contribute significantly to the understanding of biofilm processes at the micropore level.

1.1. Background

Biofilm processes are studied by researchers in a variety of fields (cf. [7] for a review). These include the biofilm accumulation on heat exchanger tubes, water and wastewater conduits, teeth and gums, intestines, the detachment of microorganisms from biofilms in cooling towers, extraction of minerals from ores mediated by biofilms and immobilized microorganisms in biotechnological industries.

Mathematical models addressing biofilm processes have been developed for saturated soils and aquifers [2], porous media [8], and closed conduits [24]. Models have also been proposed for the initial colonization of a substratum [11], mixed population [15], and monopopulation biofilms [1]. A two-dimensional model of microscale transport and biotransformation in porous media that couples the Navier–Stokes equations, advection and diffusion of a nonreacting chemical substrate, and an existing model of biofilm processes is developed in [8].

In the models mentioned above, the segregation of biomass into discrete cells and EPS is ignored in favor of modeling the biomass as a continuously distributed population. In contrast, the microscale model presented in this article represents the microbes in the biofilm system as discrete entities. Each kind of model has its own advantages. By representing cells discretely it is possible to more accurately model changes in the local geometry brought about by adhesion of cells to a substratum or by cell aggregation. This is important because it influences local flow and this in turn influences transport of cells and substrate. A detailed description of the fluid flow can lead to a greater understanding of the role of hydrodynamic forces on the dynamics of cell–cell and cell–substratum bond formation and destruction. Also, by modeling cells at this level, one has complete control over individual cell specifications regarding adhesivity, reactivity to stimuli, consumption of substrates, and so on, rather than only being able to specify these in an average sense at the population level. Detailed analysis of these characteristics could be used to provide parameter estimates for continuously distributed population models.

Platelet aggregation during blood clotting has many similarities with biofilm formation. Platelets are small cells suspended in the blood. They are normally not adherent to other platelets or the blood vessel walls. However, when the vessel wall is injured, platelets adhere to the injured tissue, and release chemicals that can make nearby platelets sticky. As a consequence, aggregates of platelets may form along the injured portion of the wall. As with biofilm development, the rate and extent of aggregation depend on cell and chemical transport by the fluid; the growth of aggregates in turn influences the local fluid dynamics; and fluid dynamic forces can limit the growth of aggregates and can, in fact, cause portions of an aggregate to break away from the wall. Discrete cell models of platelet aggregation based on the immersed boundary method were developed in [12, 14]. The methods presented in the current paper combine features of those models with features of cell motility and chemotaxis models developed in [10].

Bacteria swim by rotating flagella driven by reversible motors embedded in the cell wall (for review of bacterial motility of cf. [3]). The majority of bacterial swimming studies have focused on peritrichously flagellated bacteria, particularly *E. coli*. The motion of these organisms can be described in terms of run intervals during which the microbe swims approximately in a straight line interspersed with tumbles during which the organism undergoes random reorientation. During run intervals, the cell's flagella rotate in a counterclockwise direction forming a coherent helical bundle. When the flagella rotate in the opposite direction, the flagellar bundle unravels causing the cell to tumble. For *E. coli* the run and tumble intervals are exponentially distributed with means $\approx$1s and $\approx$0.1s, respectively, in isotropic medium [5]. Chemotactic bacteria sense temporal changes in concentration levels of chemical attractants and repellents. The direction of rotation depends upon chemoattractant concentration levels at the cell site over a time interval of up to 4 s [4]. If the concentration level of an attractant is increasing, a bacteria responds by reducing its tumbling probability [6, 19]. Thus, mean run times are longer when bacteria swim up a chemoattractant gradient. The immersed boundary method has been used to model the motility of eucaryotic organisms [13] and to model the swimming and chemotaxis of individual and small populations of bacteria based on a simplified swimming mechanism [10].

In Section 2 we describe a microscale mathematical model of biofilm processes which includes a mechanism for simulating bacterial swimming and chemotaxis, a model of microbial substrate consumption, and a model of cell–cell and cell–wall adhesion. In Section 3, we describe the computational algorithm and in Section 4 we describe simulations of several *idealized* biofilm processes. These include simulations of the initial colonization by a single species in a straight channel, chemotaxis in a straight channel, and the initial colonization of a channel with an expansion domain. A numerical convergence study is included in the Appendix.

2. MATHEMATICAL FRAMEWORK

The evolution of a biofilm system in a fluid filled microchannel or micropore depends upon the fluid motion induced by motile bacteria, the background flow, substrate advection and diffusion, and microbial uptake. Growth of a biofilm changes the geometry of the fluid domain and hence the fluid flow. The initial formation of a biofilm depends on the transport of cells to the substrata. In the nonturbulent flows characteristic of many biofilm systems, which include typical flows through porous media, this transport is due in large part to cell motility, both random motility and that in chemotactic response to a chemical substrate. In addition, microbial swimming induces local changes in the flow which affect the transport of the chemical substrates. Below we present a system of coupled nonlinear equations which describes a model biofilm system.

We assume that the fluid dynamics are governed by the Navier–Stokes equations,

$$\rho(\mathbf{u}_t + (\mathbf{u}\cdot\nabla)\mathbf{u}) = -\nabla p + \mu\nabla^2\mathbf{u} + \mathbf{F} \tag{1}$$

and

$$\nabla\cdot\mathbf{u} = 0, \tag{2}$$

which describe the balance of momentum and conservation of mass in a viscous incompressible fluid. Here, ρ is the fluid density, $\mathbf{u}$ is the fluid velocity vector, p is pressure, and μ is the fluid viscosity. The term $\mathbf{F}$ is the force density (force per unit area in two dimensions) that the microbes and pore walls exert on the fluid. As will be made clear below, the support of $\mathbf{F}$ is localized in thin layers surrounding each immersed microorganism and pore wall. It is *only* through this term that the fluid experiences the presence of the microorganisms and walls.

Contributions to the force density term $\mathbf{F}$ arise in several ways: First, the body of each microbe and the walls of the fluid pore are modeled as neutrally buoyant elastic boundaries, and fluid-induced deformation of these boundaries generates restoring forces which act on the fluid to try to reverse the deformation. Second, $\mathbf{F}$ includes forces which model the flagellar beating which propels motile microorganisms. Last, $\mathbf{F}$ includes forces due to the cell–cell and cell–substratum attraction and repulsion.

The cell body of each microorganism is modeled (in two dimensions) as an elastic ring, whose configuration is defined by the function $\mathbf{X}_i(s, t)$, where s is a Lagrangian label (e.g., arclength with respect to an equilibrium configuration), t is time and i denotes the ith microbe. The boundary force per unit length $\mathbf{f}_{\text{cell}(i)}(s, t)$ at each point on the ring is a function of the current ring configuration and consists of a tangential elastic spring force and a normal bending-resistant force. These are designed to preserve the size and the shape, respectively, of the ring. Unlike ameboid cells, bacterial cells walls are relatively rigid. In our simulations, the stiffness constants associated with the cell ring are chosen to reflect the stiffness properties of a bacterial cell wall. This ''immersed boundary force'' is transmitted directly to the fluid and gives a contribution of $\mathbf{F}$ which we call $\mathbf{F}_{\text{cell}(i)}$:

$$\mathbf{F}_{\text{cell}(i)}(\mathbf{x}, t) = \int_{\text{microbe}} \mathbf{f}_{\text{cell}(i)}(s, t)\delta(\mathbf{x} - \mathbf{X}_i(s, t))\, ds. \tag{3}$$

Here, the integration is over the points of the ring and δ is the two-dimensional Dirac delta function. Note that the volume of the cell body is maintained by the incompressibility of the enclosed fluid.

The pore walls are modeled in a manner similar to the microbe rings, that is, as neutrally buoyant elastic filaments immersed within the fluid. However, these walls cannot move freely since they are tethered to fixed points in space by stiff elastic spring forces. We define $\mathbf{f}_{\text{wall}(i)}(s, t)$ to be the boundary force per unit length on the wall and define the fluid force density contribution $\mathbf{F}_{\text{walls}}$ from it in a manner analogous to Eq. (3):

$$\mathbf{F}_{\text{wall}(i)}(\mathbf{x}, t) = \int_{\text{wall}} \mathbf{f}_{\text{wall}(i)}(s, t)\delta(\mathbf{x} - \mathbf{X}_i(s, t))\, ds. \tag{4}$$

We note that this representation of the walls makes it easy to change the geometry of the pores.

Recall that bacterial motility consists of a sequence of runs and tumbles. Bacterial swimming during the runs is achieved through the action of one or more flagella. In our model of bacterial motility and chemotaxis, the flagella are *not* explicitly represented as immersed elastic structures. Instead, a simplified set of forces is applied to the fluid at points ''behind'' the cell body to represent the forces generated by a flagellum. A detailed explanation for this simplified propulsion mechanism is given in [10]. In this model, we localize the swimming forces of the physical flagellum at two distinct points. The placement of these two points behind the cell body can be correlated with the wavelength and the amplitude of a virtual flagellum (see Fig. 1). These ''point'' forces are distributed to the fluid by the use of a smoothed two-dimensional δ-function, δ_s. Our particular choice of the smoothed δ_s function used in the numerical method is given in Section 3. Expressed with respect to a moving frame of reference whose origin is at the centroid of a microbial body of radius R_{cell} and whose $\mathbf{x}$-axis is aligned with the flagellar axis, the equation for the swimming force field $\mathbf{F}_{\text{swim}}$ is

$$\mathbf{F}_{\text{swim}}(\mathbf{x}, t) = \sum_{j=1,2} \mathbf{fs}_j\, \delta_s(\mathbf{x} - \mathbf{x}_j). \tag{5}$$

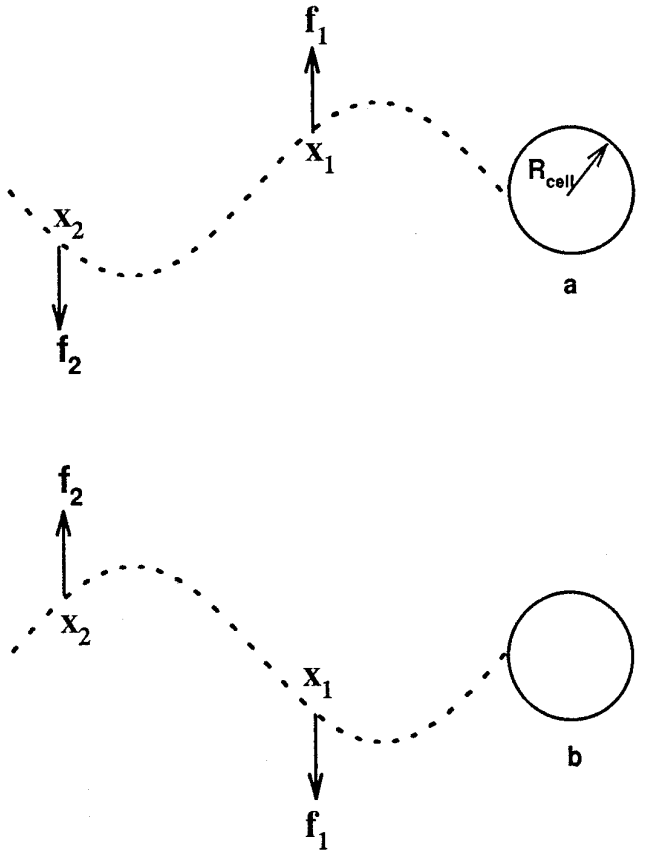

FIG. 1. Schematic representation of two-dimensional microbe. The flagellum is represented by Stokeslet force distributions at $\mathbf{x}_1$ and $\mathbf{x}_2$. The point forces $\mathbf{f}_1$ and $\mathbf{f}_2$ are orthogonal to the flagellar axis as shown in (a) for one half of the flagellar cycle and in (b) for the second half.

The vectors $\mathbf{x}_j$ and $\mathbf{fs}_j$ are given by

$$\begin{aligned} \mathbf{x}_1 &= (-R_{\text{cell}} - 3\lambda/8, \alpha), \quad \mathbf{x}_2 = (-R_{\text{cell}} - 7\lambda/8, -\alpha) \\ \mathbf{fs}_1 &= (0, F_s), \qquad\qquad \mathbf{fs}_2 = (0, F_s), \end{aligned} \tag{6}$$

for $t_0 < t < t_0 + \tau/2$ and by

$$\begin{aligned} \mathbf{x}_1 &= (-R_{\text{cell}} - 3\lambda/8, -\alpha), \quad \mathbf{x}_2 = (-R_{\text{cell}} - 7\lambda/8, \alpha) \\ \mathbf{fs}_1 &= (0, -F_s), \qquad\qquad \mathbf{fs}_2 = (0, F_s), \end{aligned} \tag{7}$$

for $t_0 + \tau/2 < t < t_0 + \tau$. This two point model defines a two-dimensional flagellum with linear wavelength λ and amplitude α. As shown in Fig. 1, the direction of the model swimming forces is transverse to the swimming axis. The reason purely transverse force can create an axial swimming velocity can be seen in the Stokeslet velocity distribution

$$\mathbf{u}(x) = \frac{1}{8\pi\mu}\left(\frac{\mathbf{f}}{\tau} + \frac{\mathbf{f}\cdot\mathbf{x}}{r^3}\right), \tag{8}$$

where $r = \|\mathbf{x}\|$. Equation (8) is a solution to the Stokes equations

$$\begin{aligned} -\nabla p + \mu\nabla^2\mathbf{u} + \mathbf{F} &= 0 \\ \nabla\cdot\mathbf{u} &= 0 \end{aligned} \tag{9}$$

with $\mathbf{F} = \mathbf{f}\delta(x)$. The Stokeslet, the sum of parallel and radial fields, represents the flow due to a point force $\mathbf{f}$ at the origin in an unbounded fluid. At the low Reynolds numbers associated with bacterial swimming ($R \approx 10^{-5}$), based on the bacterial length and swimming speed, the Navier–Stokes equations (1)–(2) can be reduced to the Stokes equations. Thus, the velocity induced by the model swimming forces (5) is approximately the sum of two Stokeslets. The axial swimming velocity is due to the radial components of the velocity fields. In this respect, this simplified model of bacterial swimming is consistent with Lighthill's analysis of bacterial swimming [18], where it was shown that an idealized bacterial flagella produced no forces in the axial swimming direction if one neglects the drag forces of the cell body. The speed and swimming efficiency of the model microbe depend on the cell radius R_{cell}, the flagellar geometry parameters α and λ, the flagellar forcing strength F_s, and the duration of the flagellar cycle τ. In the first half of the period, where $t_0 < t < t_0 + \tau/2$, the asymmetric swimming forces produce a flow field propelling the cell body forward at an angle θ to the flagellar axis. In the second half of the period, where $t_0 + \tau/2 < t < t_0 + \tau$, the cell body moves at an angle $-\theta$ to the flagellar axis. Consequently, a single model microbe moves along a zigzag path. The effect of changing τ is to vary the amplitude of this path. The flagellar axis of each cell is rigidly attached to the cell body at the cell centroid $\overline{\mathbf{X}}$ and a designated point $\tilde{\mathbf{X}}$ on the cell ring. As a result, the swimming orientation $\overline{\mathbf{X}} - \tilde{\mathbf{X}}$ changes as the cell rotates.

The placement of the virtual flagellum above can be chosen so that, in the absence of boundaries and other microbes, a given mean swimming direction of the microbe is achieved. In the presence of boundaries and other microbes, the swimming direction of an individual cell changes gradually during the course of an individual run. The swimming direction at the start of a run is the result of a random reorientation during a tumble. Chemotactic bacteria respond to an increase over time in the local concentration of a chemoattractant c by decreasing the tumbling probability. Thus, individual run times depend upon the history of the chemoattractant concentration at the location of the moving microbe [16].

When a model microbe is first introduced, its swimming orientation is chosen randomly. During subsequent tumbles, a new swimming orientation is randomly selected. The times at which a cell tumbles are determined randomly with the tumble times drawn from an exponential distribu-

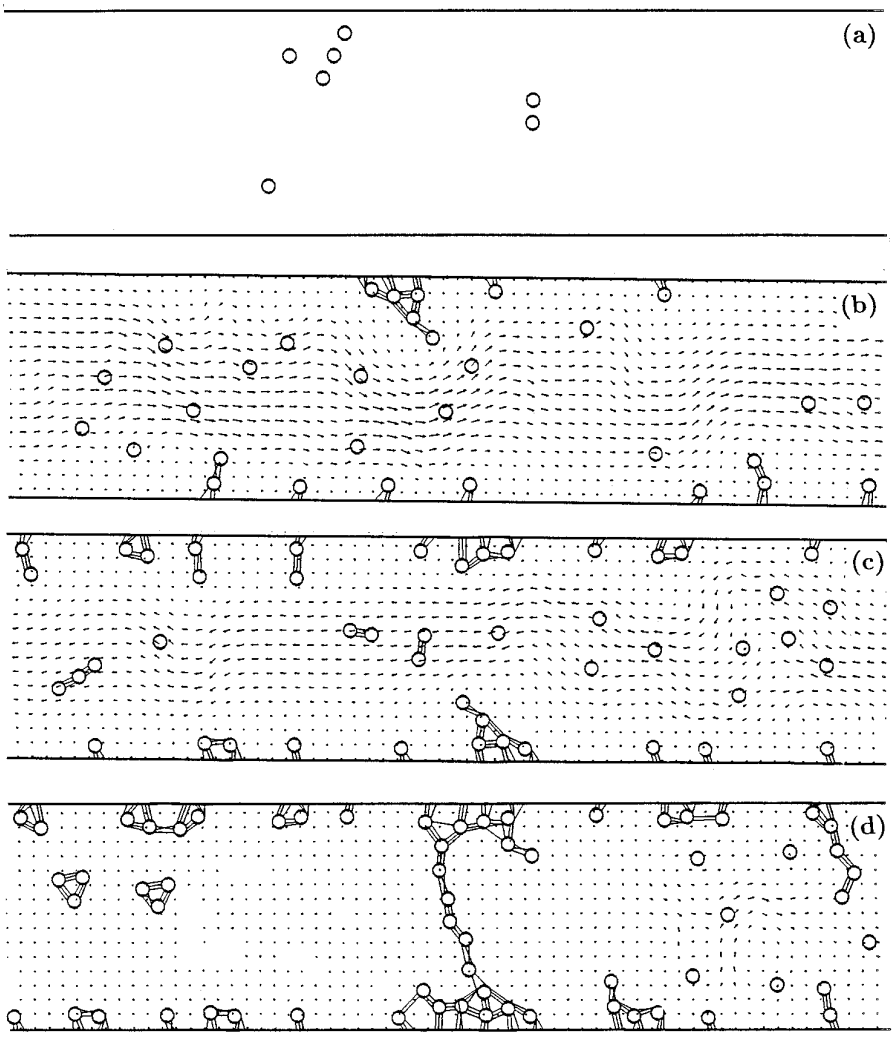

FIG. 2. Motile species with strong attachment forces: (a) $t = 0.0$ s, (b) $t = 0.30$ s, (c) $t = 0.61$ s (d) $t = 1.24$ s.

tion with the probability density function for the kth cell given by $\lambda_k e^{-\lambda_k t}$ [4]. The mean of this distribution is λ_k^{-1} and λ_k depends on the time history of the chemoattractant concentration near the microbe. The angle by which the swimming orientation changes when a microbe tumbles is chosen randomly from a prescribed distribution with a bias toward smaller angles (see [10] for details).

Cell–cell and cell–wall adhesion are modeled by the creation of elastic springs or ''links'' between points on each of the adherent entities. The model for link formation and breaking is adapted from that used in [12, 14] to model platelet adhesion and aggregation and works as follows: If the distance between the centroids of any given pair of cells is less than prescribed cohesion distance, an elastic spring may be created to link the two cells. A link is created if the number of links between these two cells has not already reached a prescribed maximum number. The mechanical properties of each spring and the cohesion distance are chosen to reflect biological and physicochemical properties of the system. Cell–wall links are formed in a similar manner if a cell's centroid is less than a prescribed distance from a wall. Detachment of cells from the biofilm is modeled by allowing the links to break when they are stretched beyond a prescribed length. An elastic link between immersed boundary points $\mathbf{X}_1$ and $\mathbf{X}_2$ gives rise to forces of the form:

$$\mathbf{f}(\mathbf{X}_1, \mathbf{X}_2)\,\delta_s(\mathbf{x} - \mathbf{X}_1) - \mathbf{f}(\mathbf{X}_1, \mathbf{X}_2)\,\delta_s(\mathbf{x} - \mathbf{X}_2). \qquad (10)$$

In this paper, the function $\mathbf{f}(\mathbf{X}_1, \mathbf{X}_2)$ is taken to be of the form $S(\mathbf{X}_2 - \mathbf{X}_1)$ with constant S, which represents a linear spring with zero resting length.

The contribution $\mathbf{F}_{cc}(i, j)$ of the adhesive links between cells i and j to the fluid force density $\mathbf{F}$ is a sum of terms like that in Eq. (10), where $\mathbf{X}_1$ lies on cell i and $\mathbf{X}_2$ lies on cell j. The adhesive links between cell i and pore wall k

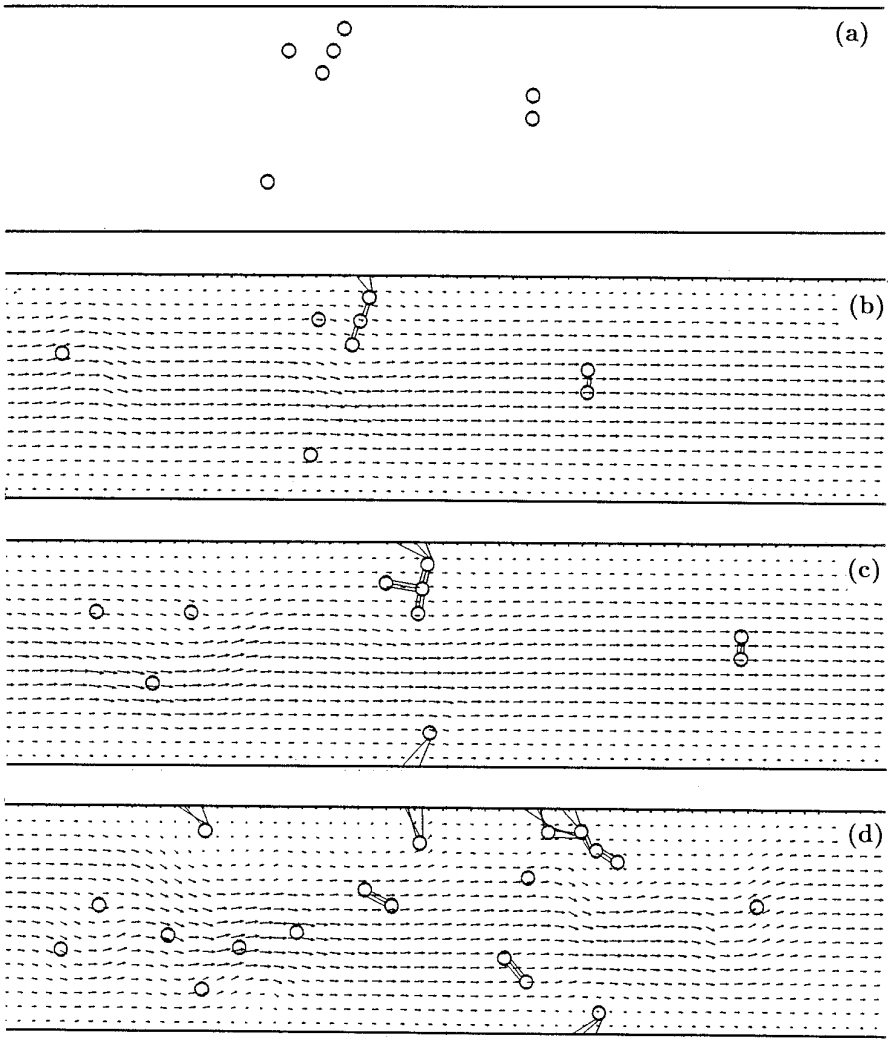

FIG. 3. Motile species with weak attachment forces: (a) $t = 0.0$ s, (b) $t = 0.006$ s, (c) $t = 0.025$ s (d) $t = 0.093$ s, (e) $t = 0.303$ s, (f) $t = 0.619$ s.

make a contribution $\mathbf{F}_{cw}(i, k)$ of the same form except that the point $\mathbf{X}_2$ lies on the pore wall.

Taken together, the various contributions to the force density $\mathbf{F}$ in Eq. (1) can be summarized in the formula

$$\mathbf{F} = \sum_i [\mathbf{F}_{\text{cell}(i)} + \mathbf{F}_{\text{swim}(i)}] + \sum_k \mathbf{F}_{\text{walls}(k)} + \sum_{i,j} \mathbf{F}_{\text{cc}(i,j)} + \sum_{i,k} \mathbf{F}_{\text{cw}(i,k)}. \tag{11}$$

Here, $i, j = 1, ..., N_c$, where N_c is the number of cells; $k = 1, ..., N_w$, where N_w is the number of channel walls.

The immersed boundaries (microbes and pore walls) influence the fluid motion through the forces we have just described. In turn, the fluid motion and continuity of the fluid velocity field give equations of motion for the points $\mathbf{X}(s, t)$ on the immersed boundaries, namely:

$$\frac{d\mathbf{X}(s,t)}{dt} = \mathbf{U}(\mathbf{X}(s,t),t) = \int \mathbf{u}(\mathbf{x},t)\,\delta(\mathbf{x} - \mathbf{X}(s,t),t)\,d\mathbf{x}. \tag{12}$$

Here the integration is over the entire domain. This can be interpreted as the usual no-slip boundary condition at a fluid–material interface.

The presence of microorganisms in the bulk fluid influences both the flow dynamics and the substrate field. The equation which describes the advection, diffusion, and consumption of a single chemical species within the fluid-filled pore is

$$c_t + (\mathbf{u} \cdot \nabla)c = D\nabla^2 c - R(c)c, \tag{13}$$

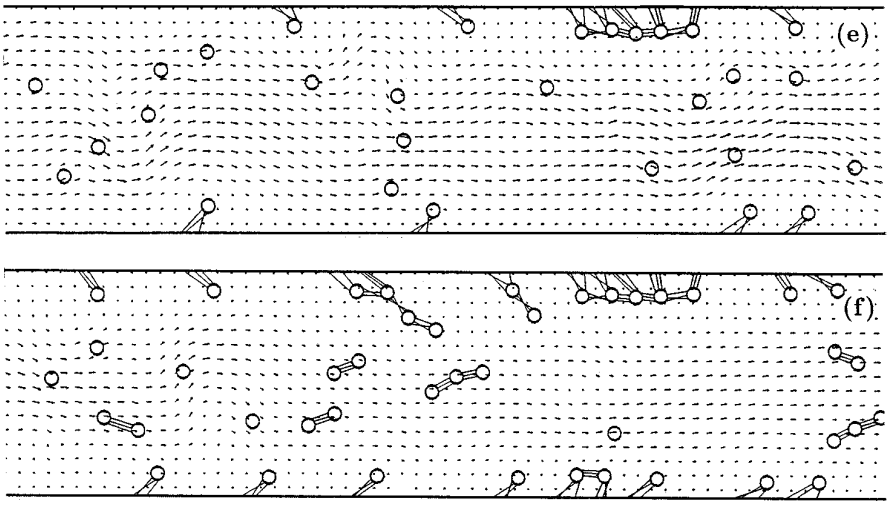

FIG. 3—*Continued*

where c is substrate concentration, D is the molecular diffusivity, and R is a consumption rate that is nonzero only near the site of each of the N_c microbes. Note that this consumption rate itself may be concentration-dependent, but in this paper we assume that it depends only on the locations of the microbes. The microbes act as localized nutrient sinks whose locations evolve over time.

This completes the description of the model system. Although it has been described within the context of two dimensions, we emphasize that the model is *not* inherently two-dimensional. The equations of fluid dynamics, substrate transport, and uptake presented above apply equally in two and three space dimensions. However, instead of modeling a cell body in two dimensions by an elastic ring made up of a series of points and springs, in three dimensions a cell body would be represented by an elastic membrane made up of a network of such points and springs. Force densities on the surface would be communicated to the fluid domain using Eq. (4), but the integration would be over the two-dimensional cell surface, and δ would be the three-dimensional Dirac delta function.

3. OVERVIEW OF COMPUTATIONAL METHOD

For computations, the fluid domain is discretized using a uniform rectangular grid, and all fluid variables ($\mathbf{u}$, p, and $\mathbf{F}$) are defined only at these grid points. Similarly, the ith immersed boundary is represented by a finite number of discrete Lagrangian points $\mathbf{X}_i(l)$ indexed by l. The immersed boundary forces are defined at these points. These immersed boundary points in general do not coincide with points of the fluid grid and communication between the immersed boundary points and the fluid grid is handled by a discretized version of the δ- and smoothed δ-functions which appear in Eqs. (3)–(5), (10), (12). The discrete δ-function δ_h is given below. The substrate concentration is defined on the same grid as the fluid variables.

The algorithm for the numerical solution of the coupled fluid–microbe–substrate system may be summarized as follows: at the beginning of each time step n, we have the fluid velocity field $\mathbf{u}^n$, the locations $\mathbf{X}_i^n(l)$ of the immersed boundary points, the current configuration of the elastic links which connect these points, and the substrate concentration field c^n. In order to update these values to reflect events that take place during this time step we:

1. Calculate the elastic force density $\mathbf{f}^n_{\text{cell(i)}}$ or $\mathbf{f}^n_{\text{wall(k)}}$ for each immersed boundary.

2. Calculate the swimming forces generated by each motile organism.

3. Calculate the cell–cell and cell–wall link forces.

4. Spread all of these forms to the grid to determine the force density $\mathbf{F}$ which drives the fluid motion.

5. Solve the Navier–Stokes equations (1)–(2) for $\mathbf{u}^{n+1}$.

6. Interpolate the fluid velocity field to each immersed boundary point and move that point at its local fluid velocity (12).

7. Use the new positions of the microbes and alter the substrate concentration in the vicinity of each microbe to account for the consumption of substrate and solve the advection–diffusion–reaction equation for c^{n+1} (13).

For step (5), we use the projection method of Chorin [9] with periodic boundary conditions. The discrete δ- and δ_s-functions used in steps (4), (6), and (7) is defined by

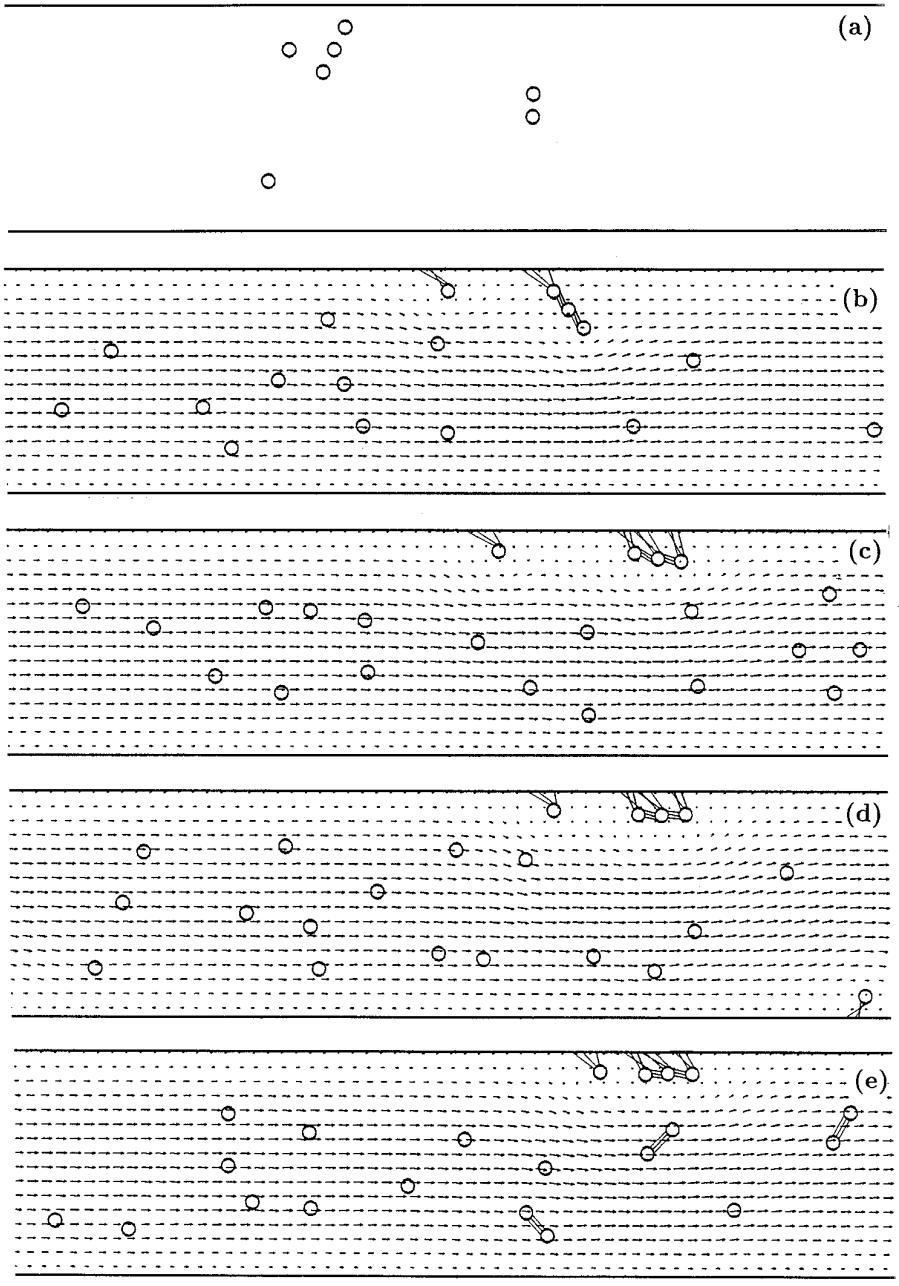

FIG. 4. Computer simulation of nonmotile cells in a straight channel: (a) $t = 0.0$ s, (b) $t = 0.087$ s, (c) $t = 0.149$ s (d) $t = 0.299$ s, (e) $t = 0.547$ s.

$\delta_h(\mathbf{x}) = d(x)d(y)$, where h is mesh width and

$$d(r) = \begin{cases} \dfrac{1}{4h}\left(1 + \cos\dfrac{\pi r}{2h}\right), & |r| < 2h \\ 0, & |r| \le 2h. \end{cases} \tag{14}$$

See [20] for details about δ_h.

The advection–diffusion–reaction equation in step (7) is solved using a finite difference method with an upwind scheme for the advection term. The substrate consumption rate function is taken to be

$$R(\mathbf{x}, c) = R(\mathbf{x}) = a \sum_{i=1}^{N_c} \delta_h(\mathbf{x} - \overline{\mathbf{X}}_i), \tag{15}$$

where a is a constant and $\overline{\mathbf{X}}_i$ is the centroid of the ith microbe.

The run and tumble process which influences the swimming forces calculated in step (2) is implemented as follows: At discrete times, $t_j = t_{j-1} + \Delta t$, the chemoattractant concentration $C_k(t_j)$ at the kth cell's centroid is determined. If $C_k(t_j) > C_k(t_{j-1})$, we set the tumbling frequency $\lambda_k = \Lambda_0$; otherwise, $\lambda_k = \Lambda_1$. The values of Λ_0 and Λ_1 determine the chemotactic sensitivity of the microbes. See [10] for more details.

4. COMPUTER SIMULATIONS

4.1. Single Species in a Straight Channel

The simulations described in this section begin with several cells placed within a fluid-filled channel. A background flow is produced by imposing a uniform pressure gradient at each grid point within the straight channel. In the absence of cells, this would induce parabolic flow.

New cells are introduced into the channel within a small rectangular buffer region at times $t_j = j\ \Delta t_C$, where Δt_c is a specified time interval. Since the background flow within the channel moves from left to right, the rectangular region is located near the left border. At $t = t_j$, a location within the rectangle is chosen randomly. If the distance between this point and each of the existing cell centroids is large enough, a new cell is introduced with a centroid at that point. The choice of Δt_C regulates the cell density within the channel. Downstream, a cell is removed from the fluid domain if the cell centroid moves into another rectangular buffer region at the far right.

Cells may be motile or nonmotile. The swimming orientation of a motile cell is specified at the beginning of the simulation or at the time of entry into the fluid domain. The swimming mechanism and run and tumble model of motility and chemotaxis have been described above. Note that cells may also be removed upstream if they progress too far to the left of the channel due to random swimming or interaction with other cells.

A cell may form as many as N_{cc} elastic bonds with another cell and up to N_{cw} elastic bonds with a channel wall. (In all of the simulations presented $N_{cc} = N_{cw} = 3$). A cell may form a new link or break an existing link at times $t_k = k\ \Delta t_L$, where Δt_L is a time interval which is specified to be longer than the timestep used in solving the transport equations to reduce computational costs, but is still short compared to the relevant time scales for the problem. When a cell forms a cell–cell or cell–wall link, the cell becomes nonmotile.

A new link is formed between two cells if the distance between cell centroids is less than CC_F. Similarly, a new link is formed between a cell and a wall if the distance from the wall to the cell centroid is less than CW_F. The new link is formed between the closest pair of unlinked immersed boundary points on the two cells or cell and wall. (At most one link is allowed to emanate from any given immersed boundary point.) A cell–cell link is broken if the length of the link is greater than CC_B. A cell–wall link is broken if the length of a link is greater than CW_B. In general the link parameters, CC_F, CC_B, CW_F, CW_B, may be functions of cell type, cell state, and the physiochemical conditions describing the fluid and pore walls. The strength, or stiffness constants, of the elastic links is set by S_{CC} and S_{CW} for the cell–cell links and cell–wall links, respectively. In the case of two-species simulations, S_{CC} and S_{CW} may depend upon the species, but in all of the simulations presented here we fix the cell–cell and cell–wall spring constants at $S_{CC} = S_{CW} = S_L$.

The evolution of this complex system depends upon the geometry of the fluid domain, the initial location of the cells, cell size, motility properties, velocity of the background flow, as well as the aggregation parameters setting cohesion distances and the strengths of the links. In the following, we investigate several scenarios in order to illustrate the capability of this computational method.

4.1.1. *Motile with Strong Links*

In Figs. 2a–d, we show snapshots from a computer simulation of a single motile species in a straight channel. The cell diameters are approximately 1 μm. Initially, all cells are motile and initial swimming orientations are randomly determined. The rectangular fluid domain is 80 μm $\times$ 40 μm. The fluid channel, bounded by immersed boundary walls within the fluid domain, is 80 μm $\times$ 20 μm and is periodic in the x-direction. The computations are performed on a 128×64 grid with $\Delta x = \Delta y$ with a fixed time step of $\Delta t = 1.25 \times 10^{-6}$ s. Each cell ring is comprised of 12 discrete immersed boundary points so that the spacing between immersed boundary points is approximately $\Delta x/2$. The closely spaced immersed boundary points prevent fluid flow across the cell membrane. The channel walls, also immersed boundaries, are each comprised of 256 points.

The microbes in this simulation follow a simple run and tumble algorithm with no chemotactic response to a substrate. We set the mean run time to be 0.25 s ($\lambda_k = 4$), which is relatively short, compared with typical run times of 1–2 s with the bacteria *Pseudomonas aeruginosa* and *E. coli*. In the absence of cells, the maximum velocity of the fluid flow in the channel is approximately 1000 μm/s. The Reynolds number with respect to the channel flow is approximately $R = 0.02$. A single cell swimming in the center of this channel, in the absence of background flow, would have an average speed of approximately 70 μm/s.

The cell–cell and cell–wall link parameters are constant for each cell with $CC_f = CW_F = 3.6$ μm. This cohesion distance is roughly 3.6 cell diameters. The decision to form a link is dependent upon the distance between cell centroids, and the decision to break an existing link de-

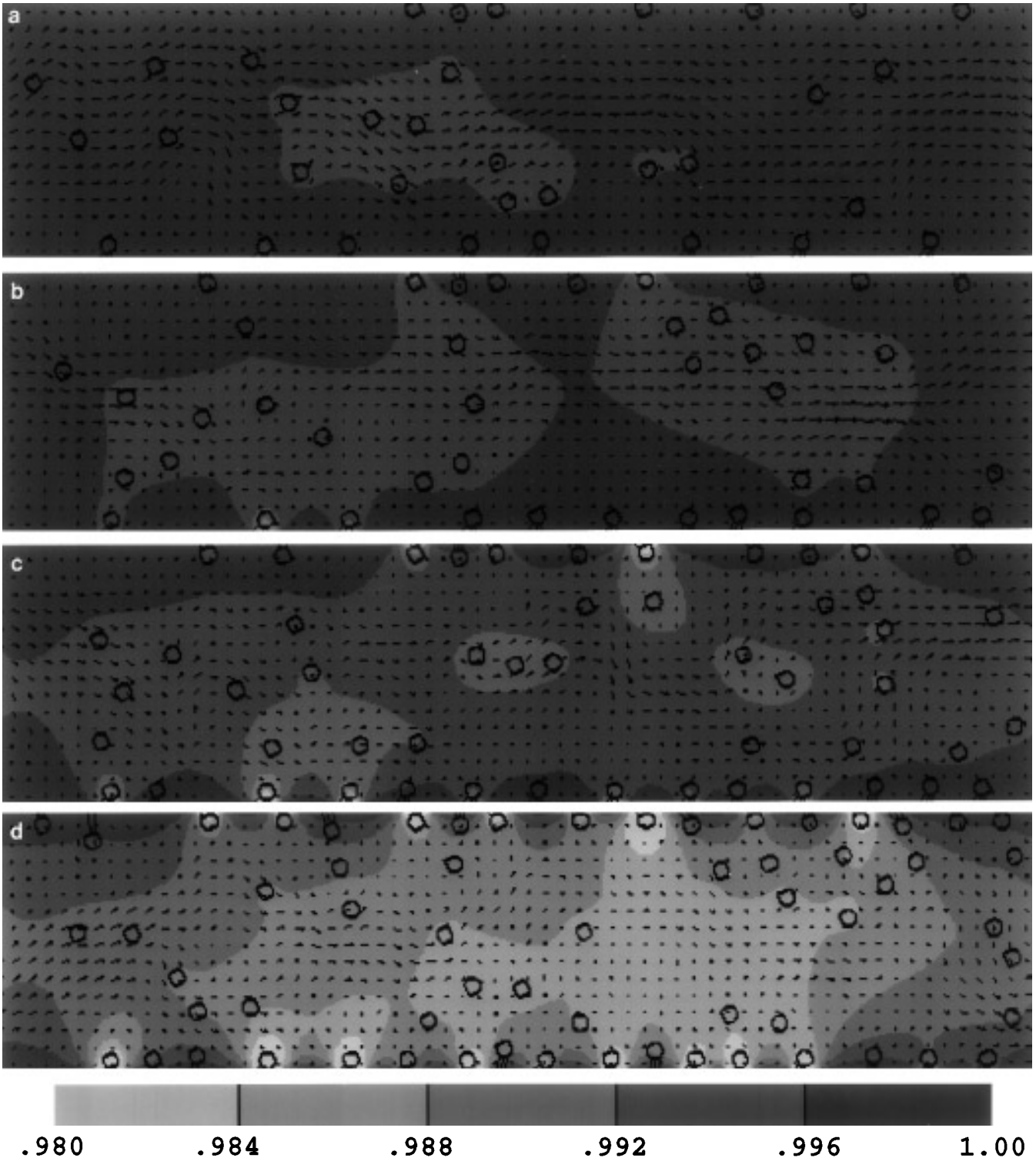

FIG. 5. Chemotactic species in a straight channel with substrate source along lower and upper channel well: (a) $t = 0.41$ s, (b) $t = 0.61$ s, (c) $t = 0.92$ s (d) $t = 1.24$ s.

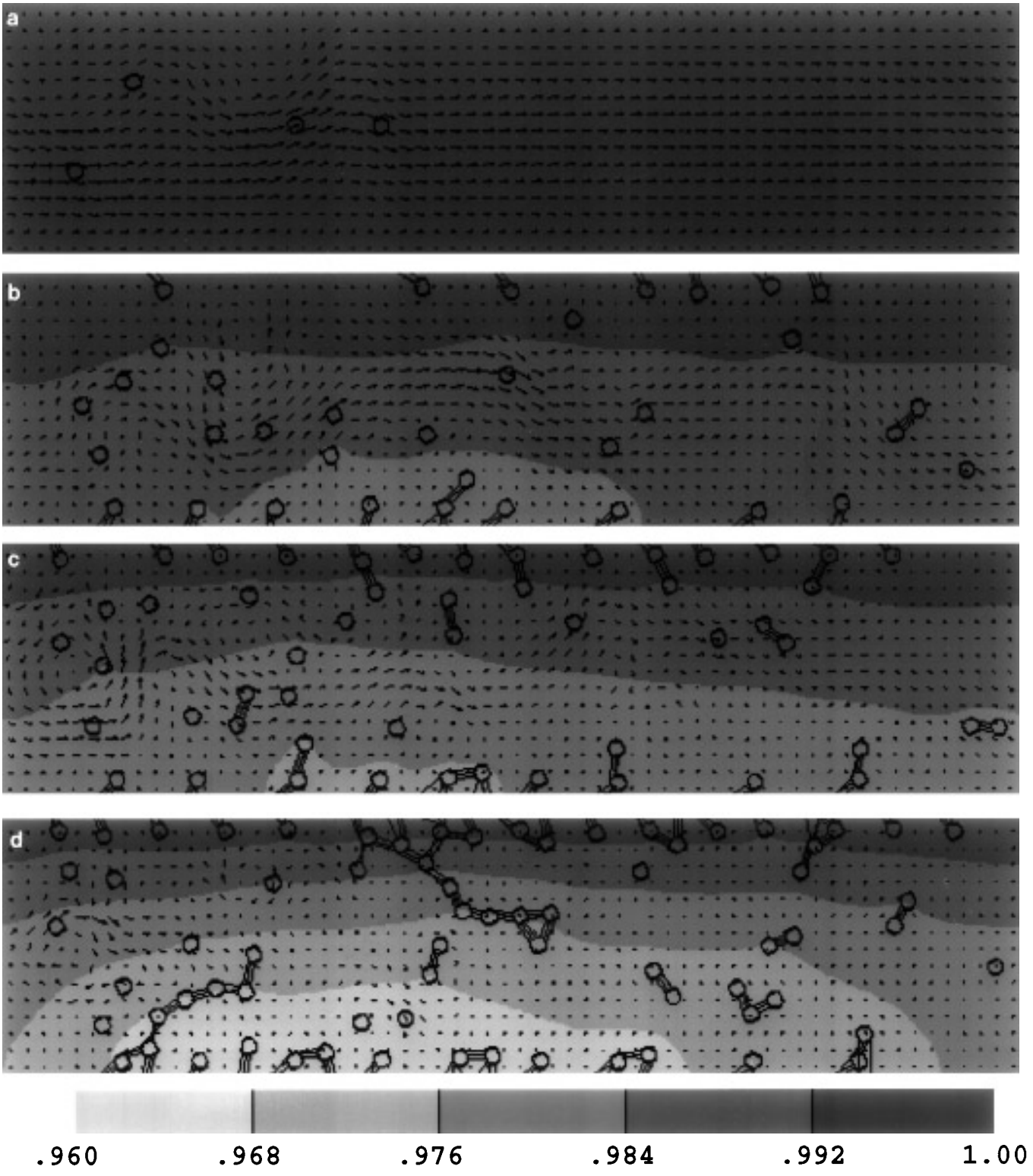

FIG. 6. Chemotactic species in a straight channel with substrate source along the upper channel wall: (a) $t = 0.05$ s, (b) $t = 0.61$ s, (c) $t = 1.23$ s (d) $t = 2.49$ s.

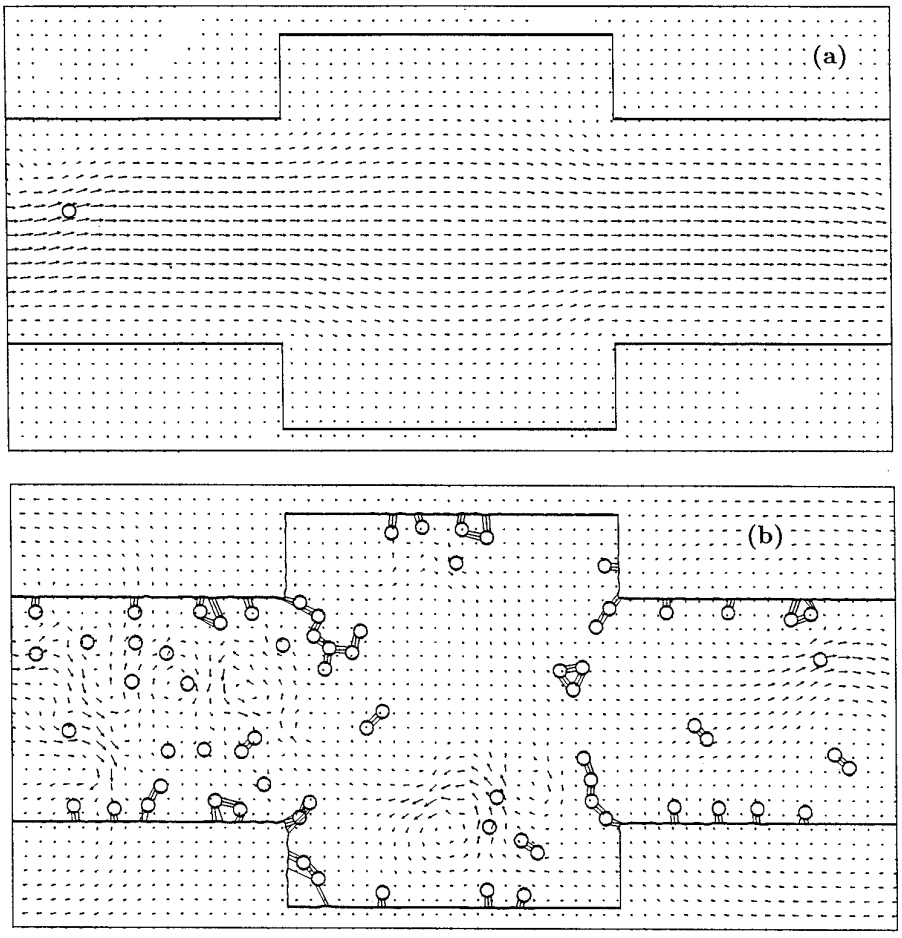

FIG. 7. Motile species in an expansion domain: (a) $t = 0.012$ s, (b) $t = 2.49$ s.

pends upon the distance between points on the rings themselves. We set the breaking distances $CC_B = CC_F - 2R_{\mathrm{CELL}}$ and $\mathrm{CW}_B = \mathrm{CW}_F - \mathrm{R}_{\mathrm{CELL}}$, where R_{CELL} is the cell radius. We note that the initial length of most links is less than this breaking distance.

The parameters chosen in this simulation produce a strong background flow, strong cell–cell and cell–wall elastic linkages ($S_L = 10^8$), highly motile cells able to swim at relatively high velocities, relatively frequent tumbling, and high cell concentrations. Since there is no chemotaxis in this simulation, cell swimming orientations are random. Thus cell motility is dominated by a diffusive-like process. The swimming speeds are weaker than the background fluid flow, so advection dominates. However, we shall see below (see 4.1.3) that even in this advection-dominated scenario, swimming is essential to the rapid formation of a biofilm. As shown in Fig. 2a, seven cells were placed initially within the channel. The V-shaped group of cells near the top of the domain immediately began to form cell–cell and cell–wall links. The attachment forces were strong enough so that cell–cell and cell–wall bonds did not break. The V-shaped group of cells, for example, formed a stable cluster on the channel wall near their initial location. During the course of this simulation (1.24 s) approximately 125 new cells were introduced into the channel and the number of cells in the channel evolved from the initial seven to 64 in the final frame. The last frame of Fig. 2 shows that attachment forces were strong enough to produce complete occlusion of the channel. A numerical convergence study for a similar simulation is included in the Appendix.

4.1.2. *Motile with Weak Links*

The initial conditions and computational parameters for our second simulation are the same as in that just described except that the stiffnesses of the cell–cell and cell–wall links are reduced by a factor of 10 ($S_L = 10^7$) (see Figs. 3a–f). Note that the V-shaped group of four cells near the top of the channel initially formed a loose aggregate, but the cell–wall links were not strong enough to hold the cells in a fixed position. These cell–wall links were broken and reformed many times as the cells were swept downstream

by the strong background current. Eventually, this group was able to form more cell–wall links and attained a stable position firmly attached to the wall as shown in Figs. 3e, f. The cells that attached along the bottom wall were also swept along by the viscous flow. After enough cells had formed attachments, the fluid velocities weakened and this allowed cells to form stable attachments by the end of the simulation. However, the attachment forces were not strong enough to generate sufficient agglomeration to form an occlusion of the channel as in the previous simulation. This simulation indicates the significance of cell adhesion forces on biofilm structure and demonstrates the global influence of local conditions.

4.1.3. *Nonmotile with Weak Links*

As shown in the two simulations above, the influence of the flagellar swimming forces in conjunction with the run and tumble algorithm can have a pronounced effect on the fluid field, making it far from parabolic. This allows many cells to move close enough to the wall to form cell–wall attachments. In Figs. 4a–d, we show snapshots from a similar simulation with nonmotile cells. The initial conditions and computational parameters are otherwise identical with the simulation shown in Figs. 3a–d. As in the previous simulations, the V-shaped group of four cells near the top immediately formed cell–cell and cell–wall links. This group was driven by the current toward the right where it eventually established a stable position. As cells moved from left to right, the trajectories were nearly horizontal until they arrived at the constriction created by the cell agglomeration at the top of the channel. Several cells did form cell–wall links as they moved toward the lower wall in this constricted region. Overall, there were far fewer cells forming cell–wall linkages in this simulation. This simulation shows the importance of including cell motility is microscale modeling of biofilm formation.

4.2. Chemotaxis with Saturated Walls

As described above in Section 3, chemotaxis of a swimming bacterial cell depends on the parameters Λ_0 and Λ_1. If $\Lambda_0 = \Lambda_1$, the cells have fixed mean run times of $1/\Lambda_0$. If $\Lambda_1 < \Lambda_0$ the cells swim preferentially up a substrate gradient. In this experiment, $\Lambda_0 = 4$ and $\Lambda_1 = 0.1$. The cells tumble much more frequently if they do not experience an increase in the substrate concentration at their centroid. In the simulation reported in this section, the substrate concentration was fixed at $c = 1$ (saturated-wall) at the upper and lower channel walls, with periodic boundary conditions on the left and right. Initially, the substrate concentration $c = 1$ was uniform throughout the channel. Here, we allowed cell–wall attachments but not cell–cell attachments ($CC_f = 0$). Otherwise, all of the system parameters were the same as in Section 4.1.1. A sequence of snapshots from this run is shown in Fig. 5. As the simulations progressed, the substrate concentration became spatially inhomogeneous due to microbial uptake and this provided a chemotactic bias toward the walls. The substrate diffusion and uptake rate parameters were $D = 10^{-5}$ cm^2s^{-1} and $a = 0.01$ s^{-1}. Although the initial substrate concentration was uniform, a boundary layer developed near the channel walls with much lower substrate concentration levels in the bulk fluid. This result demonstrates the importance of chemotaxis on biofilm creation and suggests that biofilms can preferentially form so as to sequester the substrate.

4.3. Chemotaxis—Saturated Upper Wall

In this simulation both cell–wall and cell–cell links are permitted. Moreover, the substrate concentration is fixed at $c = 1$ (saturated-wall) at the upper wall only, and Neumann conditions (insulated-wall) are imposed on the lower wall ($\partial_y c = 0$) with periodic boundary conditions on the left and right. In this simulation, there are initially no cells within the channel. Otherwise, the system parameters are the same as in the previous example. Figure 6 shows a sequence of snapshots from this simulation. As a consequence of substrate consumption and the substrate boundary conditions, an approximately vertical gradient in the substrate concentraton developed. This induced a bias in the microbial swimming toward the top wall. By the end of this simulation the number of cells in the ''biofilm'' on the upper wall far exceeded the number on the lower wall. As in the previous simulation, a boundary layer develops around the saturated wall with reduced substrate levels in the bulk fluid.

4.4. Expansion Domain

The representation of channel walls as immersed boundaries facilitates the treatment of irregular fluid domains. Since fluid flow depends on the geometry, surface irregularities may influence the formation of biofilms. As mentioned earlier, Chen *et al.* [8] developed a model of biofilm formation in porous media based on microscale transport and biotransformation in a microchannel with an expansion. In this section we describe a simulation using our model in a similar fluid domain. The fluid channel with expansion, shown in Fig. 7, is 80 μm in length. The 20 μm-wide channel is increased in width by 15 μm in the expansion domain. The expansion domain itself is 30 μm long. As in the simulations for a straight channel, a background flow is induced by imposing a pressure gradient within the channel. Aside from the changes in geometry, the parameters for the simulation shown in Fig. 7 are identical to those in Section 4.1.1. In this simulation, the cells are motile but not chemotactic. As shown in Fig. 7b, the microbes may attach preferentially to the corners of the expansion chamber contiguous with the

TABLE I

Convergence Study of Fluid Velocity Fields

		t_1	t_2	t_3	t_4	t_5	t_6	t_7	t_8
A	$\frac{\|\mathbf{u}_{256} - \mathbf{u}_{128}\|_1}{\|\mathbf{u}_{256}\|_1}$	0.095	0.154	0.044	0.056	0.076	0.073	0.080	0.069
B	$\frac{\|\mathbf{u}_{256} - \mathbf{u}_{64}\|_1}{\|\mathbf{u}_{256}\|_1}$	0.190	0.168	0.143	0.220	0.167	0.190	0.140	0.189
C	$\frac{\|\mathbf{u}_{256} - \mathbf{u}_{32}\|_1}{\|\mathbf{u}_{256}\|_1}$	0.332	0.386	0.346	0.354	0.315	0.353	0.346	0.345
	A/B	0.500	0.321	0.308	0.255	0.455	0.384	0.571	0.365
	B/C	0.572	0.435	0.413	0.621	0.530	0.538	0.405	0.548

main channel. This indicates the potential importance of channel irregularities on biofilm deposition.

5. CONCLUSION

In this paper, we have described a computational model based on the immersed boundary method for studying the complex biofilm system on a microscale level. The simulations shown here illustrate the model's capability of investigating the dependence of biofilm formation on cell motility paramters, cell adhesivity, chemotaxis, microbial consumption, as well as local geometry. As shown in Sections 4.1.1 and 4.1.2, a change in the local cohesion forces can have a dramatic effect on the global biofilm formation.

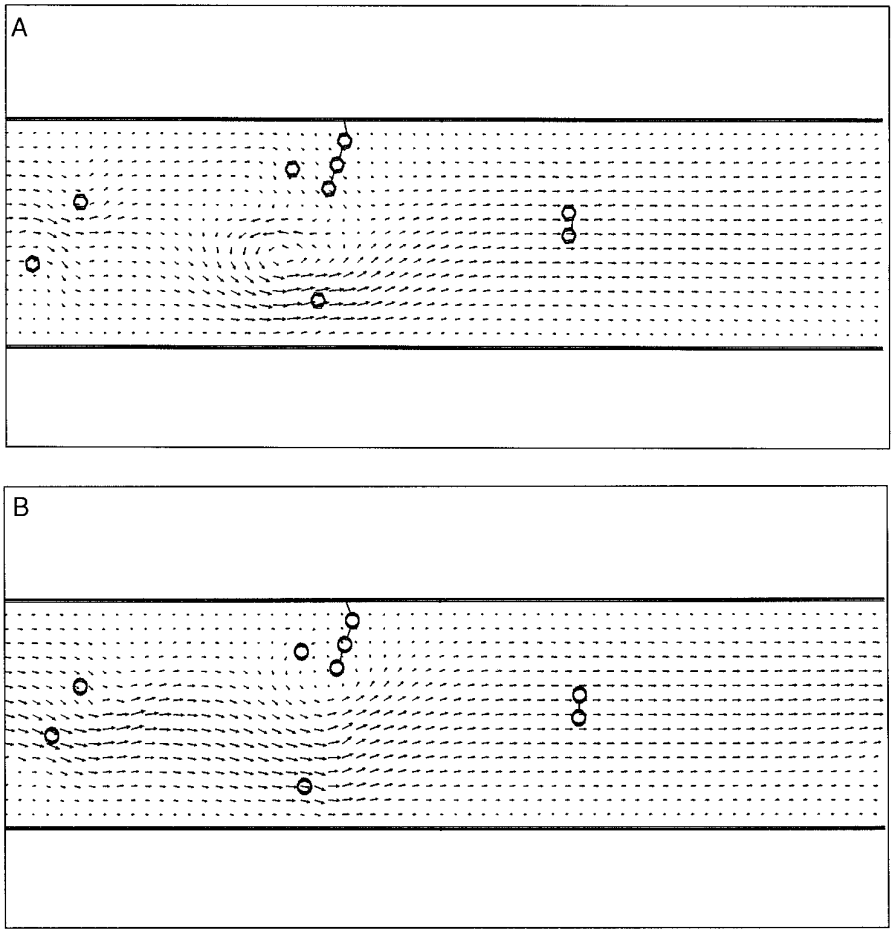

FIG. 8. Comparison of computer simulations at time $t_8 = 0.0215$ s on four grids: (a) 64×32, (b) 128×64, (c) 256×128, (d) 512×256.

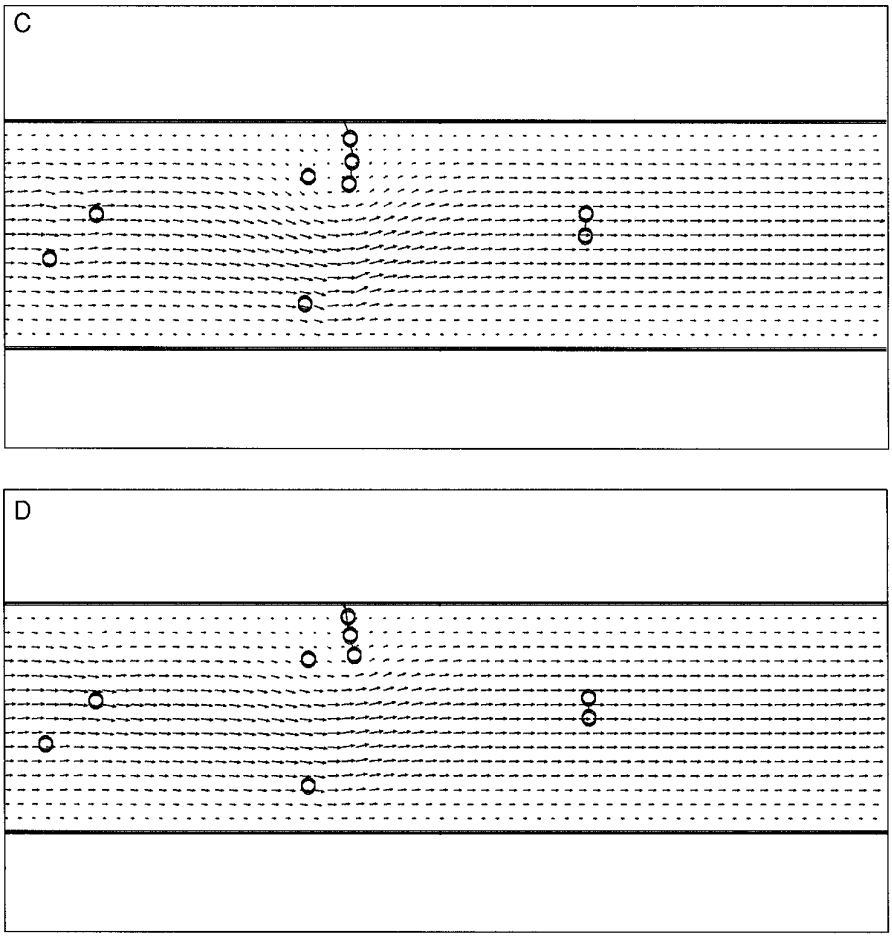

FIG. 8—*Continued*

In the absence of motility, as shown in Section 4.1.3, the rate of biofilm formation is retarded. As shown in Sections 4.2 and 4.3, microbial consumption of substrate, coupled with biofilm adherence along the channel walls can reduce substrate concentration levels in the bulk fluid even though the pore walls remain saturated with the substrate. With chemotaxis, cells may adhere preferentially to a saturated surface. Finally, the flexibility of altering channel geometry as shown in Section 4.4 facilitates the study of surface irregularities on biofilm formation. Future work includes incorporating microbial reproduction into the model, extending the model to three space dimensions and making detailed comparisons with experimental data.

APPENDIX

Previous convergence studies of the immersed boundary method have indicated that the method is first-order convergent in space [21, 23]. Peskin and McQueen [21] have demonstrated that in spatial regions away from immersed boundaries the convergence is quadratic. More recently, Roma [23] has implemented composite grid immersed boundary calculations and has shown that the ''accuracy attained by refining only the regions of the domain where the solution is not smooth is the same as if the whole computation had been performed on a uniform mesh with the resolution of the finest level used in the composite grid.'' A related numerical algorithm, the immersed interface method [17], gives higher order convergence in some situations, but a version of this method for the Navier–Stokes equations and elastic interfaces has not yet been developed.

Our goal here is to demonstrate convergence in a representative biofilm simulation. There are a number of aspects of the biofilm calculations which could complicate convergence. These include the random aspect of the cell-swimming directions and the all-or-nothing decisions made in breaking or forming cell–cell or cell–wall links. Nevertheless, we have evidence of first-order spatial convergence, consistent with previous studies.

We performed the same numerical experiment on 64×32, 128×64, 256×128, and 512×256 grids. In the three

coarsest grids, our time step is the same ($\Delta t = 1.25 \times 10^{-6}$ s), but for the finest grid it is halved ($\Delta t = 0.625 \times 10^{-6}$ s). The initial conditions are identical to those in Fig. 2a. Note that the number of immersed boundary points around a cell ring increased from six in the coarsest grid to 48 in the finest grid. Each of the cells are motile and swim with a run-and-tumble algorithm. In addition, three cells near the upper wall quickly form an aggregate. Note that when a cell is linked to the wall or another cell, it becomes immotile. Moreover, cells are introduced into the channel at fixed times and at random locations. However, these times and locations remain the same for each calculation. With this initial setup, we are including the special features of the biofilm simulations as mentioned above.

We compare the velocity fields at intervals of 1250 timesteps, up through 10,000 timesteps. (Twice as many in the finest grid calculation.) In Table I we present the relative errors with respect to the L1 norm, using the velocity field computed on the finest grid (u_{256}) as the reference: $\|u_{256} - u_N\|_p / \|u_{256}\|_p$ where $N = 32, 64, 128$, $p = 1, 2$.

The convergence ratios (A/B and B/C) are consistent with convergence that is roughly first order. Similar results (not shown) were obtained for the relative errors with respect to the L2 norm. The convergence results shown here are consistent with the results obtained by Peskin and McQueen [21].

In Figs. 8a–d we present qualitative evidence of convergence by looking at snapshots of the channel, cells, and fluid velocity field at the same time for each of the four grids. For consistency, each of the velocity fields is represented on a 64×32 grid. In Fig. 8a, we see a large counterclockwise swirl in the velocity field above the cell nearest the lower channel wall. The swirl is not seen on the finer grids. The distance between the two cells at the far left of the channel is much greater in the coarsest grid than in the three finer grids. Note that the distance between linked cells decreases as the mesh is refined and the effective cell diameter converges to the nominal cell diameter. Thus, as the mesh is refined, the cell aggregation at the top of the channel presents less of an impediment to the flow. Overall, we see a transition on the three finest grids to smoother flow and greater cell displacement toward the right as the mesh is refined.

We also compare the cell positions at the end of the simulation ($t_s = 0.0125$ s). In Table II we present the average relative error in the position of the cell centroids $\mathbf{X}_i^N$ with respect to the cell diameter D using the cell centroids $\mathbf{X}_i^{256}$ on the finest grid as the reference $(1/9D) \sum_{i=1}^{9} \|\mathbf{x}_i^{256} - \mathbf{x}_i^N\|_2$.

The ratios for the relative errors (0.462 for the finer grids and 0.664 for the coarser grids) are consistent with first-order convergence.

The computations presented in this manuscript were based on the second grid (128×64) with a time step of $\Delta t = 1.25 \times 10^{-6}$ s and run on an IBM RS6000-580 with 128 MB of RAM. The simulations presented in the appendix were run on an IBM RS6000-590. The CPU times for computing 1250 timesteps on the 590 were 43 s, 132.8 s, 707.6 s, and 8430.8 s for the four grids. This corresponds to a total run time of approximately 29 h for the 128×64 grid used for the simulation shown in Fig. 2.

TABLE II

Convergence Study of Cell Position

Relative error	t_8
$\frac{1}{9D} \sum_{i=1}^{9} \|\mathbf{x}_i^{256} - \mathbf{x}_i^{128}\|_2$	0.183
$\frac{1}{9D} \sum_{i=1}^{9} \|\mathbf{x}_i^{256} - \mathbf{x}_i^{64}\|_2$	0.396
$\frac{1}{9D} \sum_{i=1}^{9} \|\mathbf{x}_i^{256} - \mathbf{x}_i^{32}\|_2$	0.596

ACKNOWLEDGMENTS

The authors thank M. Hamilton and colleagues at the Center for Biofilm Engineering for helpful discussions. The work of R. Dillon, L. Fauci, and D. Gaver was supported in part by DOE Grant FG-01-93EW53023. The work of L. Fauci was supported in part by NSF Grant DMS-9501048 and an Alfred P. Sloan Foundation Fellowship. The work of D. Gaver was supported in part by a NSF National Young Investigator award, BCS-9358207. The work of A. Fogelson was supported in part by NSF Grant DMS-9307643. The work of R. Dillon was supported in part by a NSF Postdoctoral Research Fellowship DMS-9508815.

REFERENCES

1. R. Bakke, W. G. Characklis, M. H. Turakhia, and A-I Yeh, "Modeling a Monopopulation Biofilm System: *Pseudomonas aeruginosa,*" in *Biofilms*, edited by W. G. Characklis and K. C. Marshall, (Wiley, New York, 1990).
2. P. Baveye and A. Valocchi, *Water Resour. Res.* **25,** 1413 (1989).
3. H. C. Berg, *Ann. Rev. Biophys. Bioeng.* **4,** 119 (1975).
4. H. C. Berg, *Random Walks in Biology*, expanded edition (Princeton Univ. Press, Princeton, 1993).
5. H. C. Berg and L. Turner, *Biophys. J.* **58,** 919 (1990).
6. D. A. Brown and H. C. Berg, *Proc. Natl. Acad. Sci. U.S.A.* **71,** 1388 (1974).
7. W. G. Characklis and K. C. Marshall, "Biofilms: A Basis for an Interdisciplinary Approach," in *Biofilms*, edited by W. G. Characklis and K. C. Marshall (Wiley, New York, 1990).
8. B. Chen, A. Cunningham, R. Ewing, R. Peralta, and E. Visser, *Numer. Methods for PDE's* **10,** 65 (1994).
9. A. J. Chorin, *Math. Comput.* **22,** 745 (1968).
10. R. Dillon, L. Fauci, and D. Gaver, *J. Theor. Biol.* **177,** 325 (1995).
11. A. R. Escher and W. G. Characklis, "Modeling the Initial Events in Biofilm Accumulation, in *Biofilms*, edited by W. G. Characklis and K. C. Marshall (Wiley, New York, 1990), p. 445.
12. L. J. Fauci and A. L. Fogelson, *Commun. Pure Appl. Math.* **46,** 787 (1993).

13. L. J. Fauci and C. S. Peskin, *J. Comput. Phys.* **77,** 85 (1988).
14. A. L. Fogelson, *J. Comput. Phys.* **56,** 111 (1984).
15. W. Gujer and O. Wanner, in *Biofilms*, edited by W. G. Characklis and K. C. Marshall (Wiley, New York, 1990).
16. D. A. Luffenburger, *Microb. Ecol.* **22,** 175 (1991).
17. R. J. LeVeque and Z. Li, *SIAM J. Numer.* **31,** 1019 (1994).
18. J. Lighthill, *SIAM Rev.* **18**(2), 161 (1976).
19. R. M. MacNab and D. E. Koshland, *Proc. Natl. Acad. Sci. U.S.A.* **69,** 2509 (1972).
20. C. S. Peskin, *J. Comput. Phys.* **25,** 220 (1977).
21. C. S. Peskin and D. M. McQueen, *J. Comput. Phys.* **81,** 372 (1989).
22. P. J. Reynolds, Y. I. Chang, and T. F. Yen, *Appl. Environ. Microbiol.* **55,** 2280 (1989).
23. A. M. Roma, Ph.D. thesis, Department of Mathematics, New York University, 1996 (unpublished).
24. S. Szego, P. Cinnella, and A. B. Cunningham, *J. Comput. Phys.* **108,** 246 (1993).